



Water storage estimation in ungauged small reservoirs with the TanDEM-X DEM and multi-source satellite observations

Victoria Vanthof*, Richard Kelly

Geography and Environmental Management, University of Waterloo, 200 University Ave W, Waterloo, ON, N2L 3G1, Canada



ARTICLE INFO

Keywords:

Semi-arid hydrology
TanDEM-X DEM
Sentinel-1
CubeSats
Remote sensing of small reservoirs

ABSTRACT

Monitoring small water bodies (< 50 ha) is difficult due to their size, limiting accurate assessments of surface water (SW) resources required for agricultural production and watershed hydrology. In environments where livelihoods depend on surface-water storage (SWS) structures, satellite altimetry-derived water levels are often unavailable. Therefore, seasonal reservoirs require a robust and cost-effective approach for estimating SWS. To approximate SWS throughout a typical environmental setting where irrigation reservoirs are found, we investigate the utility of TanDEM-X digital elevation model (DEM) to extract bathymetry of seasonal reservoir structures. Empirically-derived SWS relationships are combined with estimates of SW area from radar and multi-source optical satellites to illustrate the potential for rapid SWS estimation using satellite-based SW extent as input. Two application examples illustrate the approach: (i) estimating the maximum volume of water in a southern Indian river basin for two monsoon seasons; and (ii) a time-series analysis using a high-volume of satellite observations to show the cycle of water (inflow and outflow) at the reservoir scale. SWS volumes at water levels below 1.5 m were estimated within an absolute volume error range of 6–8%. This study illustrates the applicability and challenges of using satellite remote sensing observations to continuously monitor reservoir SWS. Despite the cloud independent capability for operational monitoring of SW area, Sentinel-1 data should be combined with frequent and high spatial resolution CubeSat observations for hydrometric monitoring of reservoirs to reduce observation errors. Furthermore, we highlight the multi-sensor approach (optical and radar) to achieve high spatio-temporal resolution monitoring of small reservoirs over large spatial scales.

1. Introduction

Lakes and reservoirs are important components of the terrestrial hydrological system, though they only account for ~3.7% of Earth's surface (Verpoorter et al., 2014). Freshwater stored by reservoirs is critical for meeting global drinking water and irrigation needs (Döll et al., 2009; Gao et al., 2012; Van Den Hoek et al., 2019). Timely reservoir surface-water storage (SWS) monitoring is therefore critical for effective water resource management (e.g., flood control, drought mitigation and agricultural irrigation), and of immediate concern given predicted increased water stress from climate changes and population increases (Vörösmarty et al., 2000, 2010). In semi-arid regions where rainfed agriculture is the dominant source of livelihood and where water availability limits crop production, estimates of reservoir SWS storage are critical. Globally, however, few small reservoirs are continuously monitored (Alsdorf et al., 2007).

Civilizations in sub-Saharan Africa, Asia and Latin America have thrived in environments with large climatic variability by

implementing traditional rainwater harvesting (RWH) and groundwater extraction technologies (Mialhe et al., 2008; Van Den Hoek et al., 2019). RWH reservoirs were designed to cope with inter-annual variability in precipitation by extending water availability for agricultural and domestic use. They can also promote groundwater recharge (Palanisami et al., 2010). Yet, the small and fragmented nature of RWH reservoirs makes their wide-area monitoring challenging, with volume estimates subject to large uncertainties. Consequently, the hydrological potential of RWH reservoirs remains largely unknown (Bitterman et al., 2016).

To quantify water availability for understanding the impacts of RWH reservoirs on river basin hydrology, SWS must be monitored systematically and consistently (Bitterman et al., 2016). Traditionally, the reservoir SWS has been estimated using in-situ water levels calibrated to bathymetric maps. However, this approach is challenging over wide areas, particularly in regions where hydrological stations are unavailable. Therefore, the estimation of water volume in small fragmented systems remains an elusive goal.

* Corresponding author.

E-mail address: vrvantho@uwaterloo.ca (V. Vanthof).

Recent developments in satellite remote sensing (RS) technologies have increased the feasibility to estimate RWH reservoir bathymetry and SWS. Previously, regional scale approaches relied on shuttle radar topography mission (SRTM) digital elevation model (DEM) data at 90-m resolution (Gao et al., 2012; Sayl et al., 2017). The coarse resolution of SRTM cannot capture inundation details in small reservoirs with errors of the SRTM elevations often larger than the elevation range of artificial RWH reservoir retaining walls (Yan et al., 2015). LiDAR is the ideal dataset for reservoir bathymetry retrieval. However, its acquisition cost is prohibitive for low-income regions that depend on RWH structures.

The TanDEM-X mission provides high accuracy, regional-scale DEM for volume estimation in small RWH structures. Recent studies confirm the absolute height root-mean-square error (RMSE) to be < 2 m for the TanDEM-X DEM (Eineder et al., 2012; Wessel et al., 2018), which is an improvement over SRTM elevation accuracy (Wang and Yésou, 2018). By combining TanDEM-X data with multi-sensor surface water (SW) extent observations, it is feasible to estimate water volumes (Messenger et al., 2016; van Bemmelen et al., 2016). CubeSats have shown impressive capability for seasonal time-series monitoring of Arctic water bodies (Cooley et al., 2017, 2019) and when combined with freely available Sentinel-1 radar data, there is a significant opportunity to provide robust estimates of SW extent using operational multi-sensor observations.

This research shows how multi-temporal, multi-sensor (optical and radar) RS observations of water can be combined with the TanDEM-X DEM to estimate SWS in RWH structures during cloudy conditions in a data-scarce semi-arid environment. A volume-area (V-A) curve method is adopted since it has a demonstrated success when used with field measured DEM or SRTM DEM data to estimate water volumes for small depressional structures in specific physiographic regions such as Canada, Brazil and Africa (Karran et al., 2017; Liebe et al., 2005; Rodrigues et al., 2012). The approach is applied to seasonal small reservoirs (termed “tanks” in India) where SW areas for the smallest tanks are 0.05 km² in the Gundar River Basin (GRB). This study has three objectives:

- (i) to determine the applicability of TanDEM-X DEM for the generation of V-A relationship(s) for small reservoir structures;
- (ii) to examine the suitability of Sentinel-1A (S1-A) radar images and PlanetScope (PS) optical images to extract SW extent for volume estimates; and
- (iii) to demonstrate the reliability of the time-series volume estimation by combining radar and optical SW extent estimates with V-A relationships to inform stakeholders of the true hydrological potential of small reservoirs to support agricultural practices (in terms of water availability, droughts, etc.) in semi-arid areas.

These objectives provide the structural sub-headings used in the following Methods (Section 4), Results (Section 5) and Discussions (Section 6) sections.

2. Theoretical background

2.1. Volume estimation

Studies have proposed different approaches to calibrating satellite RS observations of SW extent directly to water volume for small reservoirs. The most successful approaches incorporate either a generalized or an actual reservoir geometry (Annor et al., 2009; Baup et al., 2014; Gao et al., 2012; Liebe et al., 2005; Sawunyama et al., 2006). The theoretical basis of the generalized approach is based on the assumption that reservoir shape can be simplified as a square-based pyramid diagonally cut in half (Magome et al., 2003). A power law expression calibrates surface area and volume within a geomorphologically homogeneous region (Annor et al., 2009; Liebe et al., 2005; Meigh,

1995; Sawunyama et al., 2006; Young et al., 2017):

$$V = aA^b \quad (1)$$

where V is the volume of the reservoir (m³), A is its SW area (m²), a is a scaling coefficient and b is an exponent indicating the rate of growth or decay. For the generalized case of a half pyramid geometry reservoir, $b = 1.5$. This is rarely the situation and instead $b > 1.5$ if the slopes of the reservoir are more convex and $b < 1.5$ if slopes are more concave. While the power model is robust for idealized hydrologic modelling (Annor et al., 2009), the a and b parameters vary with natural geomorphic heterogeneity (Liebe et al., 2005; Meigh, 1995; Sawunyama et al., 2006) with less variation in the parameters a and b when reservoirs are close together compared to reservoirs farther apart (Annor et al., 2009). It is unclear, therefore, what the spatial uncertainty of the a and b parameters is likely to be and so a key challenge lies in deriving a and b parameters that minimize error in the volume estimates from regional V-A relationships (Karran et al., 2017).

It is important to assess if the power model is suitable for particular landscape and reservoir characteristics, and whether a generalized relationship can be found irrespective of reservoir bathymetry. The accuracy of the V-A relationship is dependent on DEM accuracy (Zhang et al., 2016) which should be tested to ensure the effects of encroaching vegetation or water presence is negligible. Several irrigation reservoirs in southern India have experienced severe encroachment by invasive vegetation within the reservoir beds which degrades the accuracy of V-A relationship(s) (Reddy et al., 2018; Van Meter et al., 2016).

2.2. SW extent estimation

High temporal frequency observations of remotely sensed SW extent are needed to estimate SWS in monsoon regions. Satellite observations from active and passive sensors have been used to estimate SW extent in small reservoirs. SW extent estimation using optical imagery has a long legacy, specifically with the Landsat sensors despite their limitation from the 16-day revisit period. Planet CubeSat Dove data can provide multispectral imagery capable of observing small reservoirs daily at 3 m spatial resolution pixels under cloud-free conditions (Cooley et al., 2019). This increased temporal coverage and spatial resolution capability provides a distinct advantage over conventional visible-infrared observations because daily observations provide a greater likelihood of capturing cloud-free observations during monsoon conditions.

A detailed review of the applications for the detection, extraction, and monitoring of SW extent using optical satellite platforms can be found in Huang et al. (2018) in which a compelling case is made for the use of radar observations for hydrology monitoring as a possible alternative for, or complement to, optical imagery (Huang et al., 2018). With the recent launch of the Sentinel-1 mission and the free access to its products, satellite synthetic aperture radar (SAR) observations can image land surfaces at high temporal and spatial resolutions under near all-weather conditions, enabling continuous and repeatable observations for monitoring SW dynamics (Behnamian et al., 2017; Biorests et al., 2018; Martinis and Plank, 2018).

SAR-based water detection algorithms have been proposed to delineate water-land boundaries using grey-level threshold-based procedures (Annor et al., 2009; Bolanos et al., 2016; Clement, 2018; Martinis and Plank, 2018) where all pixel values less than a defined threshold are categorized as water for pre-defined water bodies (Behnamian et al., 2017). However, the pixel backscatter distribution for water can vary between SAR acquisitions being largely influenced by weather (surface roughness), polarization, and incidence angle. Thresholds need to be determined uniquely per scene (Bolanos et al., 2016) and ideally subdivided into regions with thresholds chosen for each region. Although grey-level threshold-based procedures are easy to implement, determining a threshold is challenging. The Otsu (1979) method, for which an optimal threshold between water and land is selected by maximizing the separability of the resultant grey-level classes, was

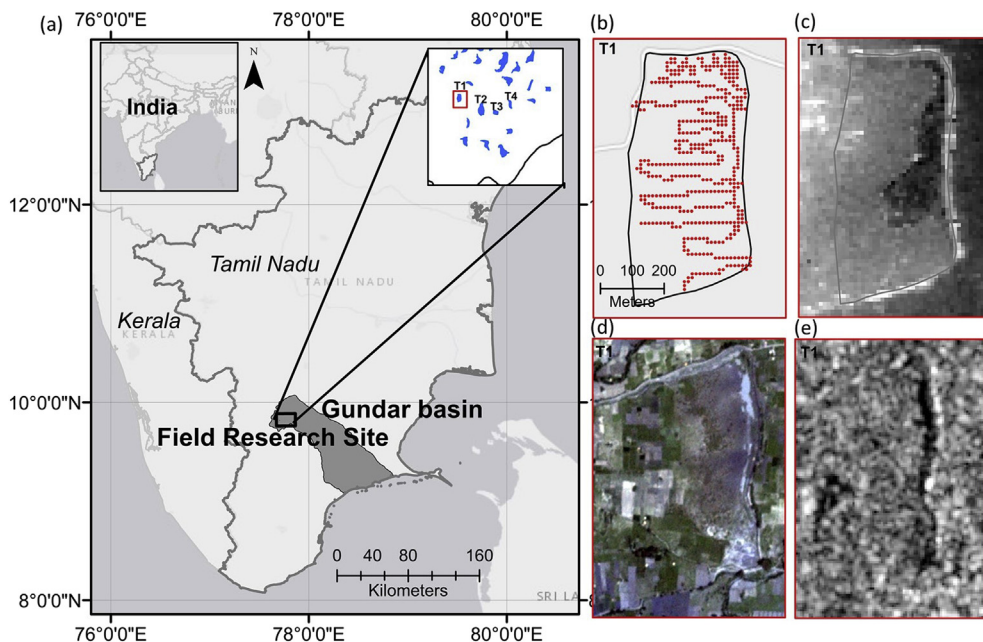


Fig. 1. (a) The location of the study area – the GRB in Tamil Nadu, India. The right inset shows tanks across the landscape with field surveyed Tanks labelled T1-T4 and T1 shown in red box in (a). (b–e) Examples of key datasets for T1. (b) Field GPS 228 elevation points, (c) TanDEM-X DEM, (d) PS imagery, (e) S1-1A imagery. (For interpretation of the references to colour in this figure legend, the reader is referred to the Web version of this article.)

selected for this work due to its proven record and tractable implementation in the Google Earth Engine (GEE) environment.

3. Study site and data

3.1. Small reservoirs in the Gundar River Basin (GRB)

A river basin with a large concentration of tanks was selected; the GRB (5647 km^2) in the south Indian state of Tamil Nadu (Fig. 1). The region is dominated by tropical monsoon climate seasons, receiving a mean annual rainfall of 770 mm/y from three distinct periods: the Southwest monsoon from June to September (25% of annual rainfall), the Northeast monsoon from October–December (50% of annual rainfall), and the dry season from January–May (25% of annual rainfall). The GRB contains hundreds of tanks developed over 2000 years ago. Tanks have been constructed across natural depressions in the landscape to capture surface runoff and rainfall. Water is impounded behind an earthen embankment (a bund) and is released through sluices into canals to be further distributed to irrigated lands. Tanks are linked in cascades, with overflow channels providing connections to tanks downstream. These connected systems form a complex hydrologic network of human-made wetlands across the landscape, ranging in size from $20 \times 10^5 \text{ m}^2$ to $80 \times 10^5 \text{ m}^2$ (Van Meter et al., 2016).

An inventory of reservoirs within the GRB was derived from cross-referencing local authority tank polygon shapefile records with other reservoir inventories. Local authority tank shapefiles were geometrically imprecise and were used only to gain an understanding of tank distribution. Of the 5647 km^2 total study area, 2314 tanks cover 9% of the basin area (Table 1). Tank size was heterogeneous with a non-linear cumulative distribution of tank area. Large tanks ($> 100 \text{ ha}$) contained 24% of the total tank water storage area despite representing only 3%

Table 1
Number of tanks in basin categorized by size and their SW area.

Tank Size, ha	Number of Tanks	Total Surface Area, km^2	Relative Water Surface Area, %
1–10	1051	50	9
11–100	1191	350	67
> 100	72	126	24
Total	2314	526	100

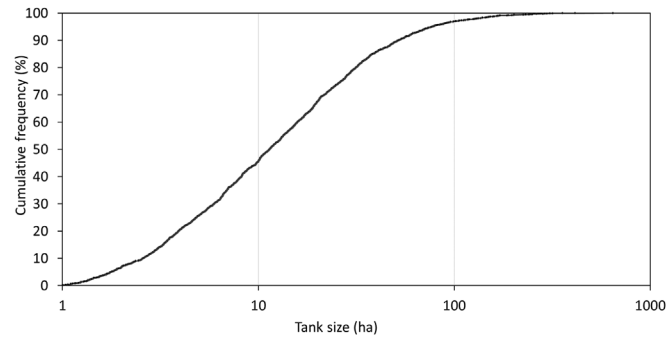


Fig. 2. Cumulative distribution of tank size ($n = 2314$). Data source: Anna University and DHAN Foundation.

of the total number of reservoirs (Fig. 2, Table 1). In contrast, mid-sized tanks (10–100 ha) accounted for 67% of the total water storage area with small tanks ($< 10 \text{ ha}$) covering 30% of the water storage area.

The maximum SW extent layer from the Joint Research Centre (JRC) Global Surface Water (GSW) dataset (Pekel et al., 2016) was used to extract accurate tank boundaries. The JRC dataset includes temporal and spatial dynamics of global surface water over a 32-year period (from 1984 to 2015) at 30 m grid cell resolution. Using a geographical information system, cells that received water in the last 32 years were intersected with the local authority tank area polygon shapefile to identify 1503 active tanks. Of these 1503 tanks, only those with maximum SW extent between 5 and 80 ha were included in this study reducing the number to 559. Further downsizing of this sample was conducted to generate a calibration dataset. A sample of 72 (13%) tanks from the total of 559 viable tanks was created by clustering the total population of tanks into four size groups within the 5–80 ha range and taking a proportional sample of suitable tanks from each group (Table 2).

This study is based on three types of data: visible-infrared and SAR data for SW area estimation, and DEM for topography. TanDEM-X DEM data were used to generate empirical V-A relationship(s) and SAR images from S1-A were used for calculating the reservoir SW area at the basin scale. V-A relationships were validated using field GPS elevation measurements and S1-A SW extents were validated using high-resolution PS data. For dense time-series volume estimation of a single

Table 2

Proportional sample from each tank size group.

Size Class	Count	Proportion	Sample Count
< 10	183	0.33	24
10–20	183	0.33	24
20–50	135	0.24	17
> 50	58	0.10	7
<i>Total</i>	<i>559</i>	<i>1.00</i>	<i>72</i>

reservoir, multi-sensor SW area estimates from S1-A, PS, Landsat-8 (L8) and Sentinel-2A (S2-A) were used. Table 3 shows a summary of the data and their purpose used in the study. Processing and analysis of SAR and optical data sources were performed in the GEE cloud computing platform with a Java API interface (Gorelick et al., 2017) and the generation of V-A relationship(s) using the Tandem-X DEM was performed using Python 2.7.

3.2. Satellite C-band SAR observations

10 m spatial resolution SAR S1-A observations were selected for this study (Torres et al., 2012). The 2015, 2017 years were selected for water monitoring because tanks received significant precipitation. A total of 46 S1-A dual-polarization (VV + VH) Interferometric Wide Swath mode products were used, delivered in Ground Range Detected High Resolution mode. Radiometrically calibrated and terrain corrected S1-A images were stored in GEE. Each scene was pre-processed with the S1 Toolbox in GEE using the following steps: (i) thermal noise removal; (ii) radiometric calibration; and (iii) terrain correction using SRTM. Additionally, in GEE, a median filter with a 4×4 window was applied to reduce speckle noise within each scene.

3.3. Satellite visible/infra-red observations

PS CubeSat satellite imagery from Planet Labs (Planet Team, 2019) were acquired for this study. PS imagery has four bands, blue (Band 1, 455–515 nm), green (Band 2, 500–590 nm), red (Band 3, 590–670 nm) and near infrared (NIR) (Band 4, 780–860 nm) and a spatial resolution of 3.125 m. For the validation of the SW extent, 14 PS Level 3A top of atmosphere radiance data product scene swaths ($\sim 225 \text{ km}^2$ each) were acquired for the listed 2017 dates: Sept. 2 (n = 8) and Oct. 8 (n = 6). These specific images matched S1-A acquisition date and contained minimal cloud cover (< 5% area of cloud-obscured fraction). An additional 27 minimal cloud covered PS images were acquired from August 2017–January 2018 to extract a time-series of SW extent for a single reservoir. GEE L8 (30 m) and S2-A (10/20 m) atmospherically corrected surface reflectance image collections were filtered to extract scenes with < 10% cloud coverage for the 2017 Northeast monsoon period covering the GRB. L8 imagery green (Band 3, 533–590 nm) and NIR (Band 5, 85–0.88 nm) bands were used along with S2-A green (Band 3, 0.560 nm) and NIR (Band 8, 0.842 nm) bands.

Table 3

Satellite and field data sources for the validation and estimation of SW extent in tank systems (Purpose: Cal = Calibrate V-A method, MA = Monitoring application). Section headings in purpose column refer to subsequent section numbers where data were applied.

Data	No. of images	Date	Provider	Purpose
Field GPS Elevation	n/a	01/Jul/2016	Topographic field survey with total station	Cal (\$4.1)
S1-A	44	01/Sep/2015–31/Dec/2015, 01/Sep/2017–31/Dec/2017	Google Earth Engine's public data catalog	MA (\$4.3)
	2	02/Sep/2017, 08/Oct/2017		Cal (\$4.2)
PS	14	02/Sep/2017, 08/Oct/2017	Planet through the Education and Research Program	Cal (\$4.2)
	27	01/Aug/2017–31/Jan/2018		MA (\$4.3)
TanDEM-X DEM	2	n/a	DLR through proposal titled <i>DEM_HYDR0751</i>	Cal (\$4.1)
L8	3	23/Aug/2017, 10/Oct//2017 29/Dec//2017	Google Earth Engine's public data catalog	MA (\$4.3)
S2-A	4	22/Aug/2017, 06/Sep//2017, 21/Oct//2017	Google Earth Engine's public data catalog	MA (\$4.3)

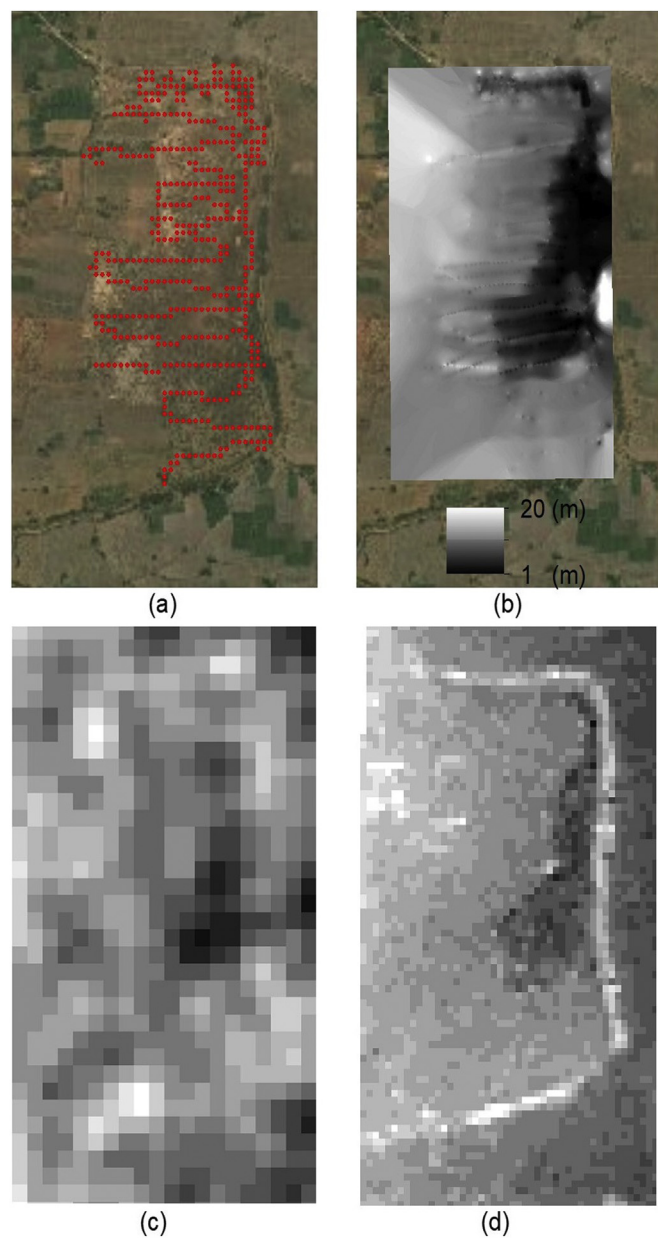


Fig. 3. (a) Field GPS data for single field tank, (b) Interpolated field GPS data from field data, (c) SRTM DEM (90 m pixels), (d) TanDEM-X DEM (12.5 m pixels).

3.4. TanDEM-X DEM product data

DEM data from TanDEM-X were used to characterize tank bathymetry assuming that reservoirs were almost empty at satellite overpass

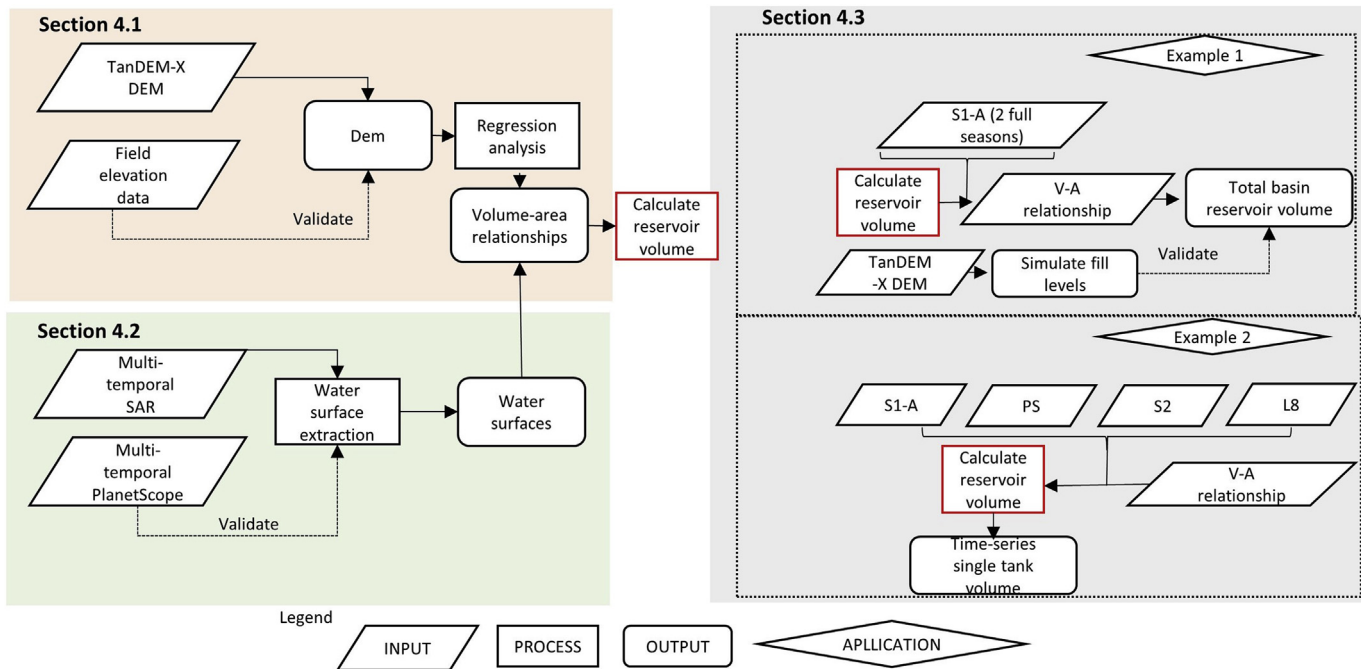


Fig. 4. Flowchart of the primary methodological steps. Sections correspond to Method Section headings.

time. DLR (German Aerospace Centre) produced a DEM from a five year (2010–2015) TanDEM-X period using InSAR methods with a spatial resolution of 10–12 m, and a relative height accuracy of 2–4 m (Eineder et al., 2009). To cover the entire of the basin, two tiles were mosaicked. Preliminary testing revealed that other global DEM products were insufficient to capture the small-scale tank topography (Fig. 3).

4. Methods

Fig. 4 shows the high-level processes applied in this study. There are two phases: (i) a calibration phase, which includes the generation of the V-A relationships and the extraction of SW area, both of which are used to provide satellite-derived reservoir volume estimates (Sections 4.1 and 4.2); and (ii) two monitoring application cases (Section 4.3).

4.1. Volume-area (V-A) model

4.1.1. Generating V-A relationships for small reservoirs

The method used to estimate volume in small reservoir structures is similar to that described in Bonnema and Hossain (2017), with the exception that TanDEM-X DEM data were used instead of SRTM DEM. For each tank, TanDEM-X DEM data provided paired volume and area estimates at 5 cm height increments from the base of the tank to the bund top (h_{max}). Only tank structures that contained negligible water and vegetation and also had a bund height of at least 3 m (typical bund height) according to TanDEM-X DEM data and high resolution (HR) imagery were used.

For the 72 sample tanks, three models were parameterized to evaluate scalability of the a and b coefficients needed for Eq. (1): the tank specific (TS) model, categorical (CAT) model and the generalized (GEN) model. For the TS model, Eq. (1) was fitted using linear least squares regression to each tank in the dataset ($n = 72$). Hence, there were 72 unique a and b coefficient pairs. Analysis of the TS model identified the a and b coefficients that best describe each tank's morphology, assessed the overall suitability of power functions to describe tank bathymetry, and estimated the water TS volume. The CAT model sought to fit a generalized model for each size category in Table 2 a and b coefficients were fitted to generate four unique equations with category-specific a and b coefficients. Analysis of the CAT model provided

an opportunity to assess the accuracy of generalized equations relative to the TS model. Finally, the GEN model provided single a and b coefficients that were fitted to all tanks, regardless of size. Analysis of the GEN model provided an opportunity to compare volume estimates for the TS and CAT models.

4.1.2. Volume accuracy V-A relationship

To estimate the error introduced by the power relation for tank estimates, the RMSE of the volume estimate for each tank was calculated between the predicted volume from each V-A model (TS, CAT, GEN) and the “reference” volume from the DEM. V-A estimates were compared with reference volume estimates at 0.05 m fill increments from empty to 100% of h_{max} . A standardized volume error, V_{ERR} (%), was calculated by dividing the RMSE by maximum tank volume (V_{max}). This enabled comparisons of error to be made between the different tanks and models regardless of tank size. In addition, V_{ERR} was calculated for two additional fill cases: 80% of h_{max} and 50% of h_{max} . These additional depths were selected to test inconsistencies in error magnitudes when the tanks do not fill completely (Minke et al., 2010). Fig. 5 shows that the largest volumetric differences occur at stage levels between 1.5 m and the spillover (located at the top of the bund at ~3 m). Studies indicate that tank water levels rarely reach spillover elevation (Young et al., 2017) and in Tamil Nadu average tank water depths rarely exceed 1.5 m (Vaidyanathan, 2001).

4.1.3. Added metrics for volume estimation

A tank's water storage capacity is defined by its bathymetry and can be calculated if bathymetry is available, typically derived at low to no fill states. However, if the height accuracy and/or spatial resolution of the DEM is low, other metrics can be invoked to explain V_{max} (Karran et al., 2017). Maximum surface area (m^2) of the tank at the maximum water height (A_{max}) can be used along with the length of the bund (B_{len}) and a dimensionless shape index to describe the shape of a tank's water surface (S_I) (Karran et al., 2017). S_I is the ratio of the tank perimeter to the circumference of a circle with the same area. Tanks with $S_I = 1$ are perfectly circular, whilst tanks with $S_I > 1$ are increasingly complex. Tank shape is an important metric because the V-A relationship is predicated on the half-cut four-sided pyramid standard bathymetry. Therefore, using the S_I metric provides an opportunity to characterize

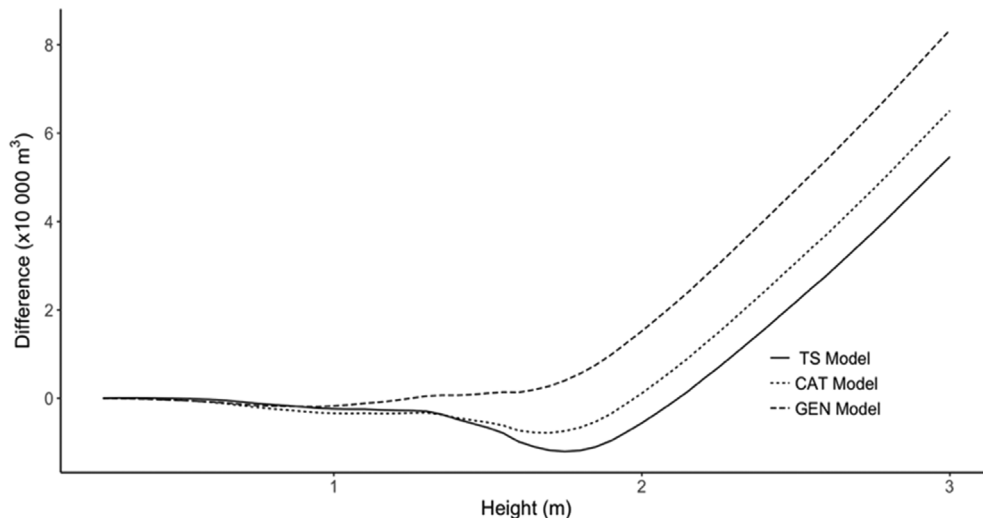


Fig. 5. Difference in predicted volume between TS, CAT and GEN models and ‘reference’ volumes from the DEM for one representative tank.

any variance from this standard (Karran et al., 2017; Minke et al., 2010). Regression and correlation analysis were performed to determine if any significant relationships exist between the morphometric variables, a , b and V_{max} . If strong correlations were found between these variables and V_{max} , they could be incorporated into the power regression relationship to improve volume estimates by accounting for increased information about reservoir morphometry.

4.2. Estimation of reservoir surface water (SW) extent

To extract SW from RS satellite observations, a multi-step procedure was followed (Fig. 6). First, for satellite visible-infrared observations, a

Normalized Difference Water Index (NDWI) was calculated for each image (Eq. (2)).

$$NDWI = \frac{(green\ band - NIR\ band)}{(green\ band + NIR\ band)} \quad (2)$$

This index is used to better distinguish open-water pixels from non-water pixels. Planet sensors only measure a narrow electromagnetic spectrum range (455–860 nm) and therefore, no modified NDWI index was applied because no shortwave infrared (1400–3000 nm) is available (Du et al., 2016). For SAR scenes, the VV and VH bands were extracted and median filtered (4×4 pixels) to reduce speckle noise.

The delineation of SW extent is performed to extract a reservoir

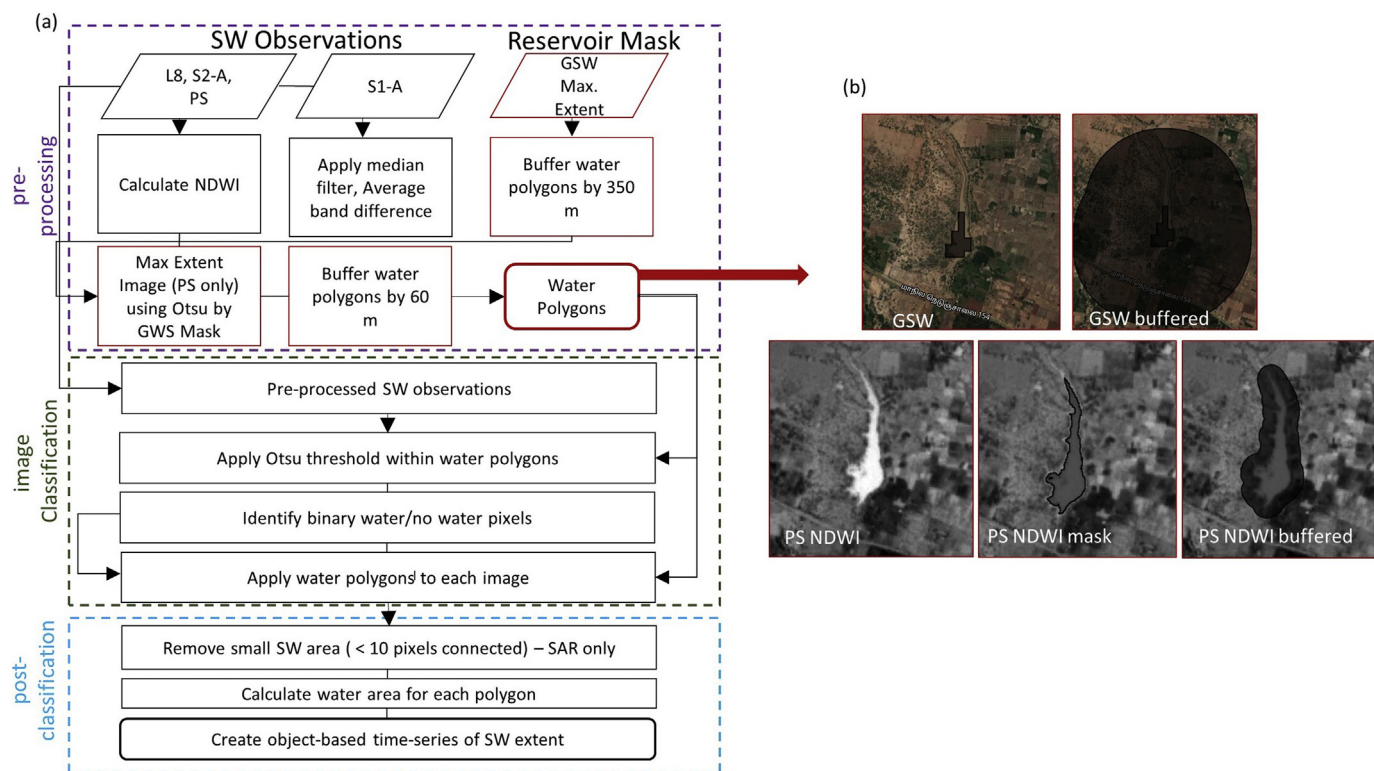


Fig. 6. (a) Water classification workflow for visible-infrared and S1-A imagery. Red squares show the steps for generating the polygon water mask layer. (b) Images show the steps for generating the polygon water mask layer. (For interpretation of the references to colour in this figure legend, the reader is referred to the Web version of this article.)

mask from a surrounding land area polygon that contained the reservoir and constrained the extraction procedure. RS-estimated small reservoir areas can be overestimated in complex environments which have water and non-water surface types present (i.e., vegetation presence, surrounding wet fields). Therefore, the GSW layer was buffered by 350 m and intersected with PS-NDWI data to extract SW from PS data. Second, the PS-NDWI classified water pixels were converted to vector polygons and buffered by 60 m (Fig. 6b). This process generates a more suitable tank mask compared to the GSW layer or manual delineation of reservoir bounds (Fig. 6b).

For each scene, a local Otsu threshold (limited by the re-defined tank mask) was used to generate unique thresholds. For PS scenes, thresholding on a local basis prior to combining PS satellite images is critical to minimize radiometric calibration and/or sensor variability between the CubeSats (Cooley et al., 2017). Masked pixels below the Otsu-defined threshold were labelled as water and above the threshold labelled as land. Each area classified as water was converted to vector format and subsequently, the SW area for each vector was calculated to generate a object-based time series of reservoir SW extent.

The SW extents were compared, and the area differences were used to compute the mean absolute error (MAE), mean absolute percentage error (MAPE) and, as used by Sawunyama et al. (2006) and Eilander et al. (2014), the Differential Area Index (DAI). The DAI is a dimensionless index comparing the area of the true estimate, here we used PS SW area compared S1-A SW area. DAI values range from -1 to 1; with values of 0 having the best match between PS SW extent and S1-A SW extent while values approaching 1 or -1 show increasing disagreement between SW extent estimates.

4.3. Monitoring water storage

Two application examples were evaluated using the 72 sample tanks and the methods described in Section 4.1 and 4.2: 1) estimation of tank volumes at the basin scale from SAR S1-A and 2) a multi-sensor time-series analysis for a single tank.

4.3.1. Evaluation of basin scale tank water volume estimates from S1-A

To test (1) with the aim of evaluating the suitability of SAR for SW mapping of tank dynamics using solely S1-A observations, a time-series of SW area was extracted using the method in §4.2. The monitoring period covered the Northeast monsoon season in 2015 and 2017 and the water dynamics of 559 tanks were assessed, although not all were used. Total water volumes were estimated for tanks that received water during this period from the appropriate power models determined by tank size category. Unfortunately, within-season tank re-filling is not captured by infrequent satellite observations. Therefore, it was not possible to evaluate the magnitude of volume estimates for all tanks in the basin. Furthermore, the TanDEM-X DEM dataset does not capture tank geometry accurately in all cases. It was necessary, therefore, to identify the tanks that were observed by S1-A to fill in both years and that were accurately characterized by the TanDEM-X DEM dataset. An extrapolation of tank fill volumes across the basin (assuming these tanks were widely distributed) could be calculated and used to test the estimates with DEM volume calculations.

The TanDEM-X DEM (for the sample testing tanks) was used to simulate fill levels to provide an approximate assessment of the volume estimates in the absence of field measurements. A subset of 34 of the 72 tanks used for the V-A calculation (§4.1) that had water in both 2015 and 2017 was used to assess basin-wide water accumulation in the tanks. These 34 tanks covered proportionally the size categories used in §4.1. For each tank, the DEM was used to estimate fill levels directly at four stage levels (0.75, 1.5 m, 2.25 m, 3 m). The median volume for each of the four size categories of the 34 tanks was calculated for each fill level and these median values were used to estimate the water volume using TanDEM-X DEM data at each of the four fill levels for the tanks that received water for the monitoring period.

4.3.2. Single tank volume estimate from multi-sensors

For the time-series application example, test (2), a high spatio-temporal resolution monitoring approach was investigated using a time-series analysis for a single tank from multi-sensor observations. A specific reservoir was selected that had the highest number of cloud-free observations to highlight the benefit of a multi-sensor observation monitoring approach. For this reservoir, SW was extracted from all available L8, S2-A, PS and S1-A data for the 2017 Northeast monsoon season. A time-series of tank storage dynamics was then estimated using the power equation for the tank size category and the SW extents.

5. Results

5.1. Volume-area (V-A) model

5.1.1. TanDEM-X Bathymetry Validation

To evaluate the TanDEM-X DEM for the purpose of bathymetry retrieval, the TanDEM-X DEM data were compared to Trimble S6 Robotic Vision Total Station GPS survey data collected at four tanks during the dry season to determine elevation accuracy and bathymetric representation. The absolute accuracy, profiles of bathymetric information for shape reproduction and the V-A relationship(s) derived from the two datasets were evaluated.

Fig. 7a shows the histogram of the differences between DEM and GPS and indicates an approximately uniform distribution with a mean close to zero. Fig. 7b provides the TanDEM-X height differences to GPS plotted against the absolute elevation of the GPS data per tank. The error is generally within a ± 1 m with no bias in difference as a function of GPS elevation. Table 4 show the MAE and the RMSE between the TanDEM-X DEM and field elevations range from 0.67 to 0.86 m and 0.98–1.47 m, respectively for the four tanks. These vertical errors of the DEM are smaller than reported accuracies of 2–4 m, providing confidence for implementing the TanDEM-X DEM to derive V-A relationships for a larger sample of tanks (Eineder et al., 2012).

The height differences were also investigated spatially between the TanDEM-X DEM and GPS elevations (Fig. 8). No spatial relationship was found between the magnitude of the error and location with a consistent error of approximately ± 1 m range across the tank bed. Fig. 8 also shows that the bund is the point of highest elevation in the TanDEM-X DEM and has an average height difference of 1.3 m with the GPS collected data ($n = 128$ heights). Moreover, the a and b parameters derived from the field data and the TanDEM-X DEM are similar (Table 4). Therefore, the strong agreement between the field GPS and the TanDEM-X elevations support the use of TanDEM-X DEM for estimating bathymetry in tank structures.

5.1.2. Tank morphometry

Based on the 72-tank proportional sample, tank morphometry is representative of various shapes and sizes of tanks that are present in southern India. B_{len} ranged from 599 to 3399 m (mean = 1305 m). V_{max} ranged from 50445 to 809678 m³ (mean = 243563 m³). Low correlations (i.e. $R < 0.7$) were found between V_{max} and B_{len} , S_1 , b , a , and A_{max} , and also between S_1 and B_{len} , b , a , and A_{max} . For Eq. (1), V-A coefficients b and a reveal information about the slope of the reservoir (the bund) and the openness of the half-pyramid tank bed, respectively. These parameters varied significantly among the 72 tanks, with the b parameter ranging from 1.1 to 1.9 (mean = 1.5) and the a parameter ranging from 1.64×10^{-5} – 1.57×10^{-1} (mean = 1.30×10^{-2}). Of the 72 tanks, 45 (63%) have b parameters that were < 1.5 , indicating more concave bathymetries (Magome et al., 2003). The small a parameters for the 72 tanks reveal that the tanks are narrow and without an evident flat middle area (Magome et al., 2003). Despite these characteristics, the ponding area generally occurs along the bund, from which the V-A relationship is developed. A strong correlation of 0.98 was observed between the a and b parameters indicating that the V-A power relationships developed for the basin (GEN or CAT) are generally

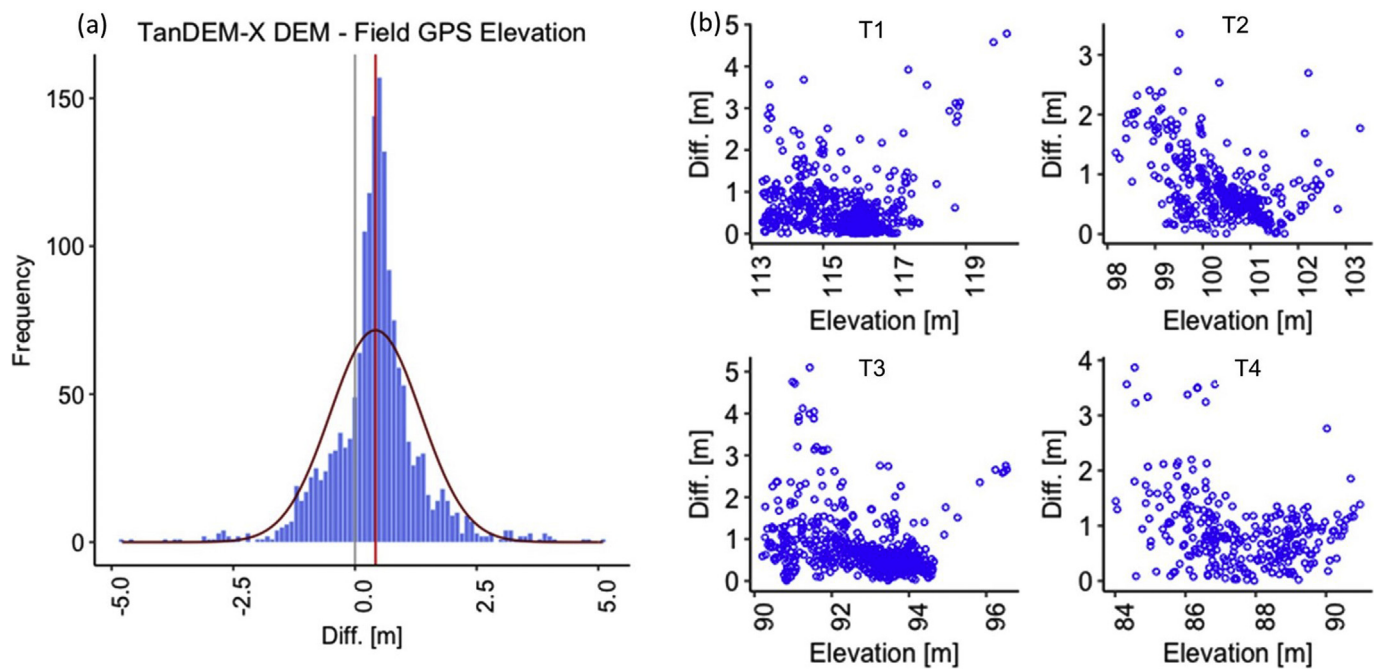


Fig. 7. (a) Histogram plot of height differences for TanDEM-X DEM minus GPS points and (b) Height differences between TanDEM-X DEM and GPS points plotted to reference GPS elevation for surveyed Tanks 1–4 (labelled T1-T4 in (b) with their location shown in Fig. 1(a)).

Table 4

: MAE, standard deviation, RMSE, V-A relationships and the R² value for four tanks comparing the TanDEM-X DEM to topographic field measurements made in 2016.

Site	Mean Absolute Error (m)	Standard Deviation (m)	RMSE (m)	Volume-Area Relationship	
				$V = a \times A^b$ from field (F) & TanDEM-X (T) data	R ² (%)
Tank 1	0.67	1.22	0.98	(F) $V = 0.00061 \times A^{1.7}$	97
				(T) $V = 0.00042 \times A^{1.7}$	97
Tank 2	0.86	1.72	1.47	(F) $V = 0.00107 \times A^{1.7}$	90
				(T) $V = 0.00156 \times A^{1.5}$	96
Tank 3	0.76	1.12	0.89	(F) $V = 0.00021 \times A^{1.6}$	94
				(T) $V = 0.00035 \times A^{1.6}$	92
Tank 4	0.80	1.50	1.26	(F) $V = 0.00861 \times A^{1.2}$	96
				(T) $V = 0.00876 \times A^{1.3}$	95

applicable.

5.1.3. V-A relationships

Using the TanDEM-X DEM bathymetry, V-A relationships for 72 reservoirs were obtained using the method described in §4.1 for low to no water conditions as verified from field GPS data. The V-A relationships for CAT and GEN tank categories are shown in Table 5, while the unique (TS) 72 relationships are not listed. Despite the variety of reservoir sizes, the generalized equation for the 72 tanks fitted the observed model with an overall R² of 95%.

5.1.4. Assessment of Volume error

While the power relationships in Table 5 have high R² values, the sensitivity of the *a* and *b* parameters to the corresponding volume estimates was assessed. The V_{ERR} (%) of volumes estimated from the three models (TS, CAT, GEN) were compared with actual volume estimates from the TanDEM-X DEM in Table 6 and Fig. 9. The data show the error differences using the DEM only for volume estimates compared with a power model developed at various spatial scales (i.e., tank scale or the combination of many tanks). In general, Fig. 9 and Table 6 show that

the CAT model had the lowest average V_{ERR} for each size category and fill level (h_{max}, 80% and 50%) and performed best. While the local TS model was expected to have the lowest V_{ERR}, it also appeared to introduce large uncertainties of volume estimation for select tanks. The basin-wide GEN model was similar in performance to the TS model. Consistently, the tanks in the smallest size category (< 10 ha) and largest size category (> 50 ha) had the highest V_{ERR} for all models. It should be noted, however, particularly for the GEN model, that the V_{ERR} is highly variable between the tank size categories, with the largest average V_{ERR} of 22% for tanks < 10 ha in size. The increased V_{ERR} for very small tanks is expected because they vary substantially in shape. Understanding the higher V_{ERR} values associated with large tanks require a larger sample size.

The *a* and *b* parameters developed for the TS, CAT, and GEN models were originally developed at a h_{max} of 3 m. Evaluating the V_{ERR} at 80% of h_{max} and 50% of h_{max} shows that the V_{ERR} decreases with fill level. This decrease is most evident at 50% of max where the V_{ERR} is 7% for the TS model. For practical application of the power regression equations for volume estimation, water levels are rarely elevated to 3 m and thus the uncertainty in the estimates is likely closer to the V_{ERR} at the 80% and 50% cases.

5.2. Estimation of reservoir surface water (SW) extent

To evaluate the suitability of S1-A for SW extent retrieval, tank SW extents were extracted from two S1-A scenes and compared with SW extents determined from PS scenes on the same satellite image acquisition date. The classification derived from the VV polarized images had a stronger correlation with the PS water mask compared with the VH polarized band images (96% compared to 91%), confirming a higher sensitivity of the VV polarization to the presence of SW in tanks.

With respect to the SW area, Table 7 shows the SW extent estimates of 92 tanks obtained from the cloud-free PS images (total of 7.57 km²) and from S1-A images (total of 6.24 km²) in 2017. S1-A observations underestimate the total SW coverage by ~18% (1.3 km²). When comparing the SW estimates at the tank level, the DAI varied substantially across the 92 tanks (Fig. 10) with an average DAI of 0.33, corresponding to an area difference of 33%. Only a small subset of tanks

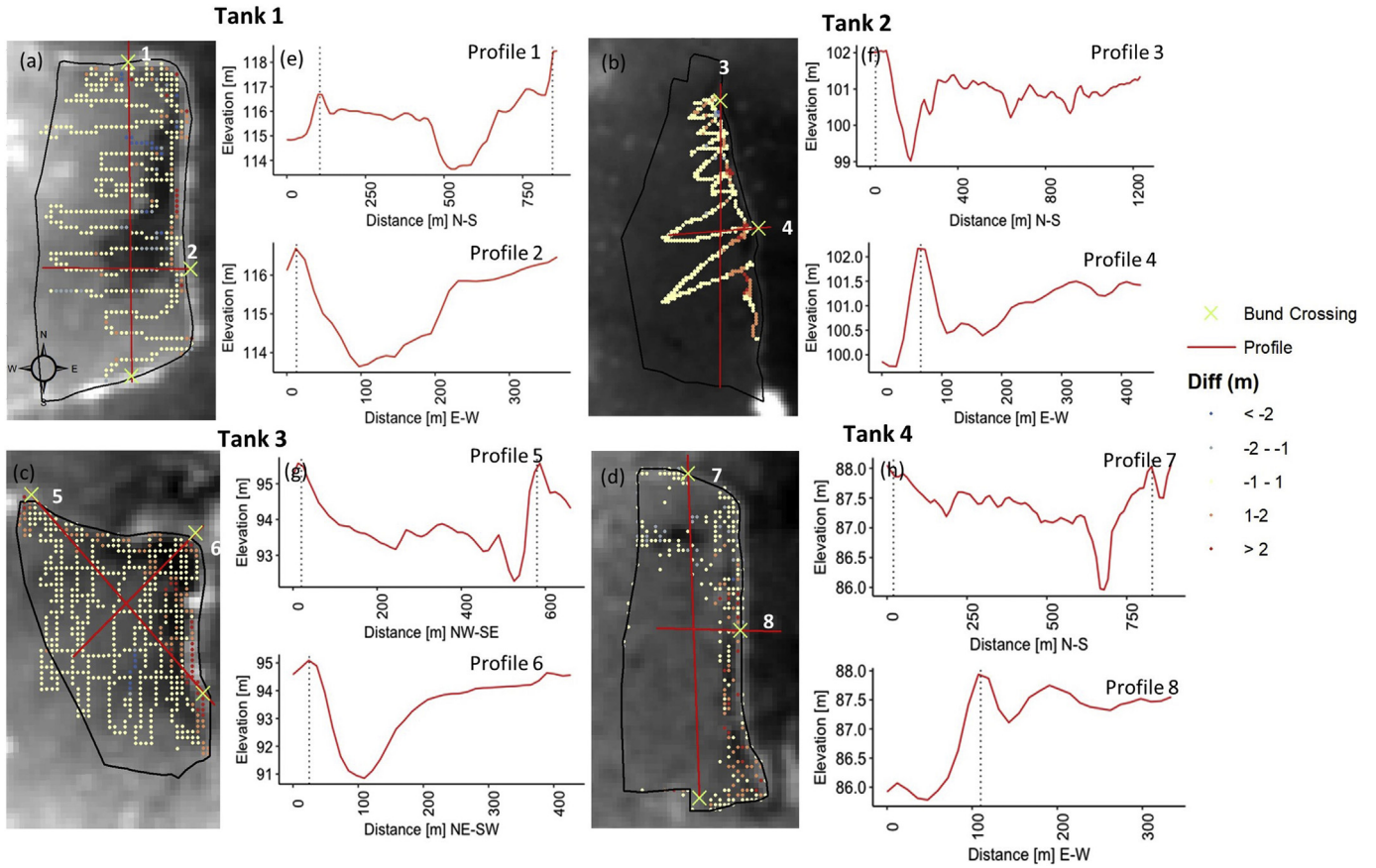


Fig. 8. (a–d) Mean height difference, TanDEM-X DEM minus GPS heights, averaged over TanDEM-X DEM pixel for Tank 1–4. (e–h) Elevation profiles extracted from TanDEM-X DEM for each tank, dotted line shows bund location.

Table 5

Generalized V–A relationships and the coefficient of determination (R^2) values for GEN and CAT models. V is the tank volume (m^3), A is the tank surface area (m^2), and a , b are parameters.

Tank Size Category (CAT)	n	$V = a \times A^b$	R^2
< 10	24	$V = 0.00277 \times A^{1.5}$	94%
10–20	24	$V = 0.00599 \times A^{1.4}$	96%
20–50	17	$V = 0.00734 \times A^{1.4}$	97%
> 50	7	$V = 0.01116 \times A^{1.3}$	95%
All (GEN)	72	$V = 0.00871 \times A^{1.4}$	95%

were overestimated by S1-A ($DAI < 0$) and the majority of tanks were underestimated compared to PS SW area. The red bars in Fig. 10 show that four tanks were completely undetected in the S1-A imagery.

To better understand the variability in SW estimates between the PS and S1-A observations, the 44 tanks with a DAI above 0.3 were visually inspected. 17 tanks fell into the DAI range above 0.6 and they all

revealed the same feature, namely that each had elongated narrow SW extents (Fig. 11a) (Fig. 11a–d). Consequently, the SW extents were mostly undetected (eight tanks showed this case) in the S1-A imagery (Fig. 11c). Tanks with a DAI between 0.3 and 0.5 either contained more moderate underestimation (Fig. 11e–h) and/or commonly displayed undetected water pixels along the border of the SW extent in the PS scenes (Fig. 11i–j).

These differences in tank SW extent are caused by the difference of spatial resolution between the two satellites and complexity in the S1-A polarization response for SW detection. PS has a spatial resolution three times finer than S1-A and typically resolves water/no water boundaries accurately. For SAR observations of small reservoirs, there is large variability in backscatter intensities from water surfaces. The surface roughness of the water is highly variable from wind and strongly influences backscatter response over time and space. Underestimation also arises when the contrast between land and water deteriorates, due to the absence of vegetation on the land surrounding a small reservoir at the end of the dry season (Liebe et al., 2009b).

Table 6

V–A model performance comparisons based on the mean (\pm standard deviation) percent volume error magnitude (V_{ERR}). ‘n’ is the number of tanks studied in each size category. V_{ERR} 80% and V_{ERR} 50% refer to the volume error at 80% and 50% of h_{max} respectively (see §4.4.1).

Tank Size (ha)	n	TS		CAT						
		V_{ERR} max	V_{ERR} 80%	V_{ERR} 50%	VERRmax	VERR 80%	VERR 50%	VERR max	V_{ERR} 80%	V_{ERR} 50%
< 10	24	17 \pm 6.8	13 \pm 5.5	8.2 \pm 3.4	15 \pm 3.9	12 \pm 3.1	7.3 \pm 1.9	22 \pm 3.4	18 \pm 32.8	11 \pm 1.7
10–20	24	13 \pm 6.4	10 \pm 5.1	6.4 \pm 3.2	13 \pm 4.6	10 \pm 3.7	6.3 \pm 2.3	14 \pm 4.3	12 \pm 3.4	7.2 \pm 2.1
20–50	17	10 \pm 5.4	8 \pm 4.3	5.0 \pm 2.7	9.9 \pm 4.2	7.9 \pm 3.5	4.9 \pm 2.1	9.0 \pm 4.1	7.2 \pm 3.6	4.5 \pm 2.2
> 50	7	16 \pm 4.6	13 \pm 3.7	8.0 \pm 2.3	15 \pm 0.6	12 \pm 0.5	7.5 \pm 0.3	18 \pm 7.0	14 \pm 5.6	8.9 \pm 3.5
All	72	14 \pm 6.6	11 \pm 5.3	6.8 \pm 3.3	13 \pm 4.5	10 \pm 3.6	6.4 \pm 2.2	16 \pm 6.6	13 \pm 5.3	8.0 \pm 2.3

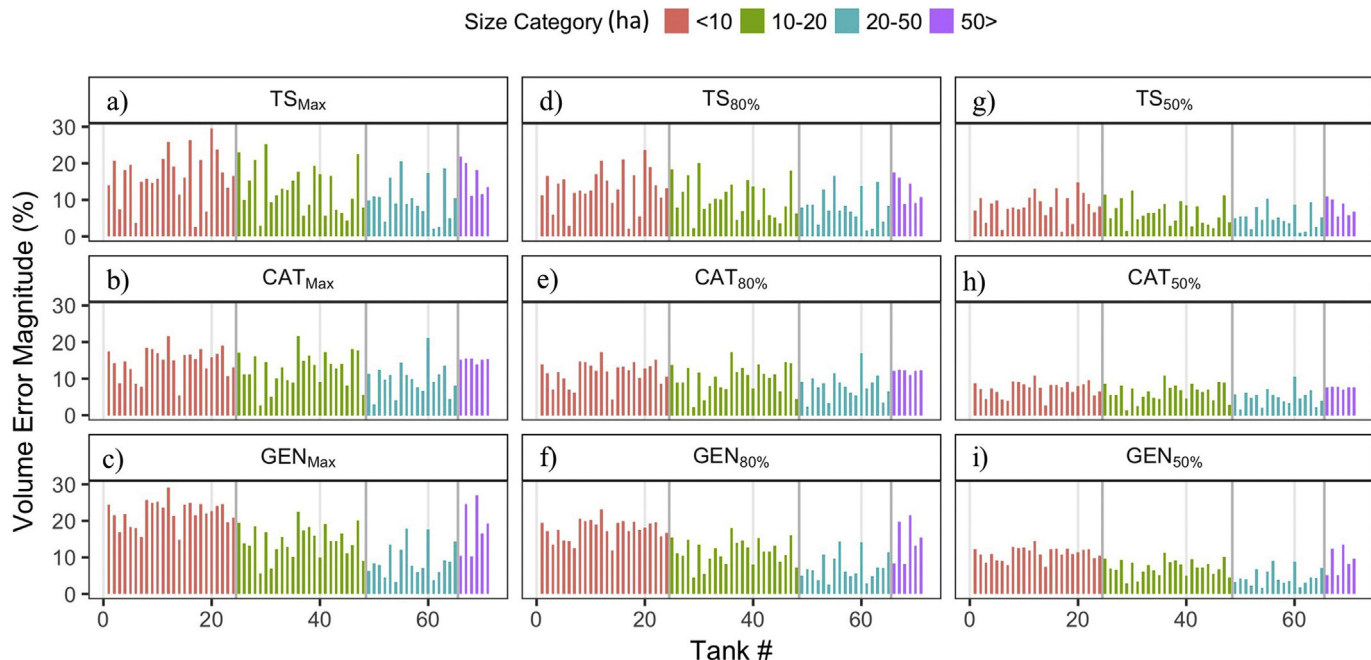


Fig. 9. Volume (V_{ERR}) error from each tank using the three different models (a–c) at h_{max} , 80% of h_{max} (d–f) and 50% of h_{max} (g–i). Bars are colour coded by size category as per the legend at the top of the figure. (For interpretation of the references to colour in this figure legend, the reader is referred to the Web version of this article.)

Table 7
Accuracy of 92 tank SW extents from S1-A compared to PS extents.

Date	n	Total PS area (m ²)	Total S1-A area (m ²)	MAE (m ²)	MAPE (% Area)	DAI
02/Sep/2017	37	2994500	2384100	18691	31	0.28
08/Oct/2017	55	4581100	3861200	22001	36	0.36
All	92	7575600	6245300	20671	34	0.33

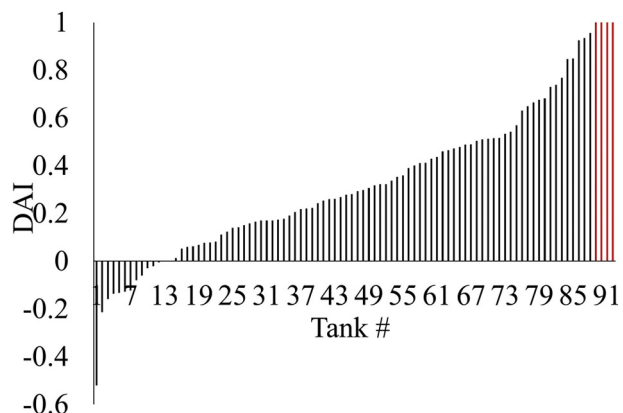


Fig. 10. DAI for 92 tanks. Red bars show tank SW extents that were not detected by S1-A. (For interpretation of the references to colour in this figure legend, the reader is referred to the Web version of this article.)

These results suggest that for tank monitoring, SAR observations are suitable under conditions similar to a tank shown in Fig. 11*i*. However, the ideal conditions are challenging to separate given the large variety in tank geometry and complexity of radar surface interactions. The degree of accuracy that small water bodies can be extracted from the radar images depends on the land–water contrast and while the DAI for several tanks is high, radar observations during cloudy conditions are still an important data source when PS observed only cloud cover. However, when implementing S1-A only for tank monitoring, a subset

of tanks will be omitted or SW extent underestimated. When translating these SW extents to volumes, the total tank volume will in turn be underestimated (Table 8). For the tank sample ($n = 92$), the difference in SW extent translates to a volume difference of 27%. In ideal conditions (the top 20% of the sample with the lowest DAI) the volume difference drops to 10%. Fig. 12 shows the SW area used in Eq. (1) and demonstrates a strong significant correlation between the tank SW extents obtained with PS and S1-A. As shown, there is 95% probability that the true best-fit line for the population lies within the confidence interval (green line) and the predicted PS tank extent from S1-A data falls between the prediction intervals with 95% probability (red line).

5.3. Monitoring water storage

V-A methods were tested in two applications to illustrate the potential and limitations in monitoring tank structures. Test (1) presents the results for maximum water volume estimation at the basin scale for the 559 tanks using only S1-A data for two high precipitation Northeast monsoon years (2015 and 2017). Test (2) focuses on a time-series analysis for a single tank from multi-sensor observations.

5.3.1. Basin scale volume estimates from S1-A

For SW area changes during the Northeast monsoon, only 49% in 2015 ($n = 274$ based on 16 S1-A scenes) and 48% in 2017 ($n = 268$ based on 28 S1-A scenes) of the tanks showed the presence of water. Therefore, despite high precipitation monsoon years, not all tanks were functioning with 177 of the tanks not showing water storage in either year. Van Meter et al. (2016) showed that many tanks are currently not operating as functional reservoirs.

Using the CAT power models to estimate water volume and the time-series of S1-A scenes for both monsoon years when observed at maximum SW extent (for tanks with water present during the season), the S1-A estimated volume is 8222995 m³ and 5129576 m³, respectively for 2015 and 2017. For the two years, the volume estimates are difficult to compare as not all the same tanks filled in the two years. For this reason, the estimated maximum volume for the same tanks ($n = 179$) that received water for both observation years are reported.

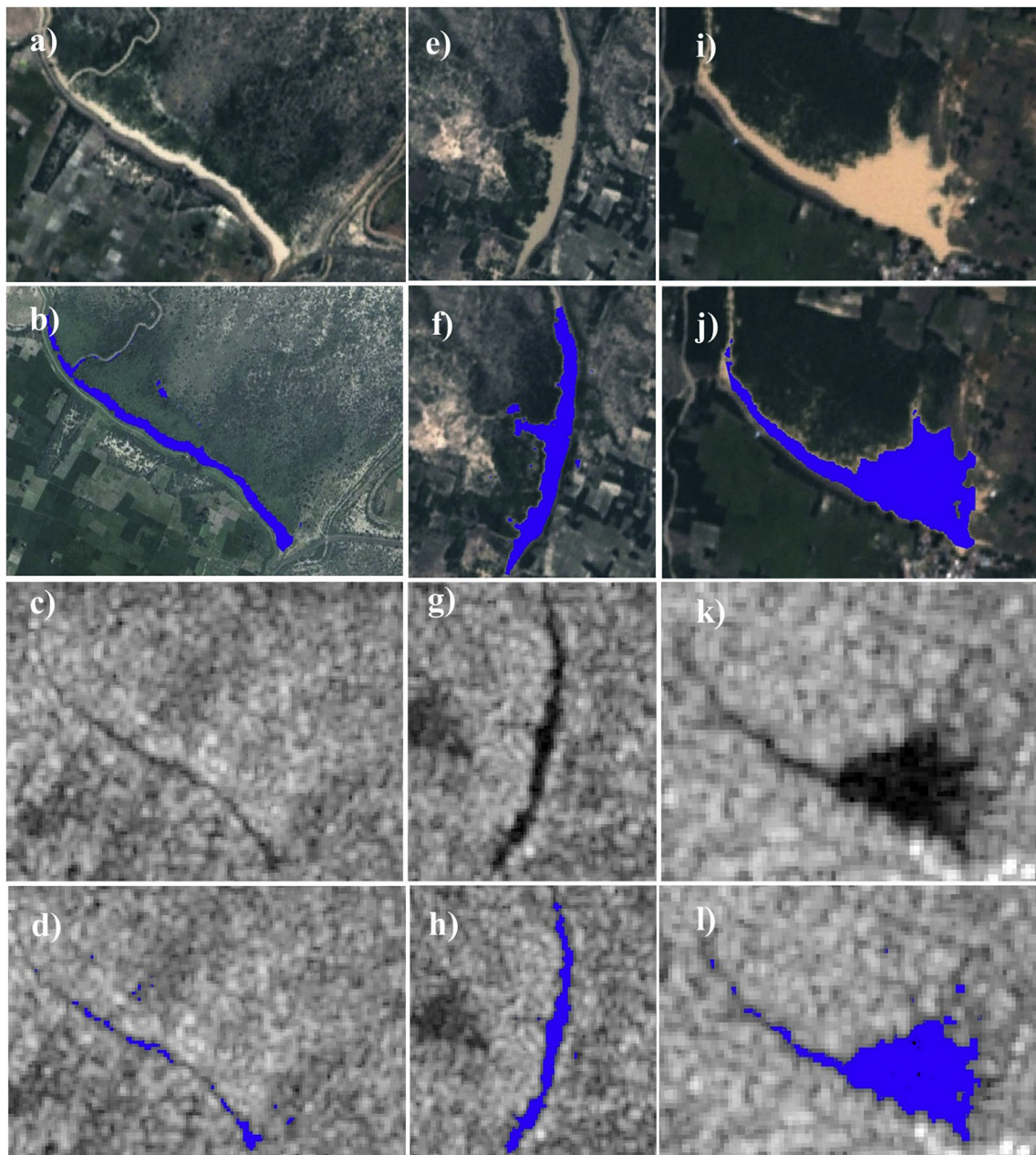


Fig. 11. Examples of the DAI for three tanks displaying variable DAI errors. (a), (e), (i) display PS true color composite (TCC); (b), (f), (j) show extracted SW area from PS on TCC image; (c), (g), (k) show S1-A scene; and (d), (h), (l) show extracted SW area from S1-A. (For interpretation of the references to colour in this figure legend, the reader is referred to the Web version of this article.)

Table 8

Tank volume total and difference between the S1-A and PS when using GEN equation from Table 5. The volume difference as a % and the standard error are listed.

# of Tanks	PS Volume (m ³)	S1 Volume (m ³)	Volume Diff. (%)	Standard Error (m ³)
All tanks (n = 92)	7547841	5511221	27	25736
Best performing 20% (n = 18)	2344445	2118480	10	11061

This revealed that between the two observation years (2015 and 2017), the total tank water volume was larger by 36% for 2015 than 2017 (6303091 m³ versus 4011419 m³ respectively). This finding is supported by Northeast monsoon precipitation estimates for 2015 and 2017 from the gridded Climate Hazards Group InfraRed Precipitation

with Station (CHIRPS) satellite product data, for which the total Northeast monsoon precipitation for 2015 was 596 mm compared with 282 mm for 2017. As noted in the validation of S1-A SW extent compared to PS SW extent, when using S1-A for tank monitoring, there are likely tanks that have been fully omitted leading to SW underestimation and so it is expected that the basin wide SW volume estimates are likely an underestimation. Cloud-free PS images were not available at the basin scale on the dates corresponding to the S1-A data, and therefore, we cannot quantify the underestimation for this sample; the validation reported in §5.2 for 92 tanks showed that the volume could be underestimated by ~27%. However, for the purpose here, to demonstrate the application of S1-A for tank monitoring, we compare two monsoon seasons for the same tank sample and therefore consider it acceptable if both years are underestimated without the absolute volume underestimation being quantified.

To contextualize volume estimate consistency, the total volume

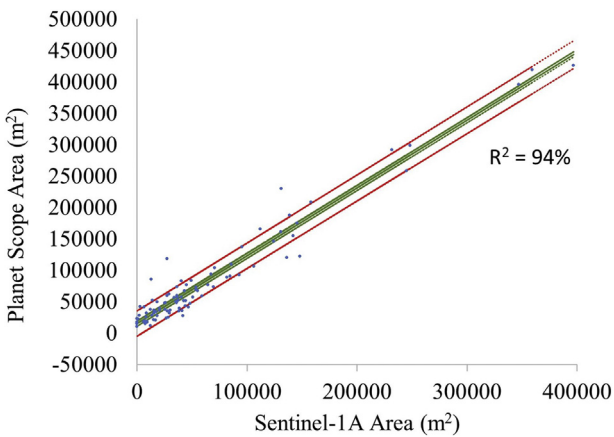


Fig. 12. Graph comparing SW extent for 92 tanks between S1 and PS. Red line equals prediction interval and green line equals confidence intervals at 95%. (For interpretation of the references to colour in this figure legend, the reader is referred to the Web version of this article.)

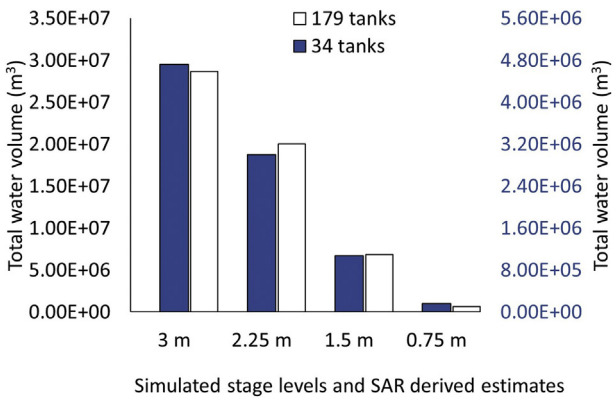


Fig. 13. Total water volume for 34 tanks with simulated fill levels at 3.0 m, 2.25 m, 1.5 m and 0.75 m (right y-axis) using the TanDEM-X DEM compared with 179 upscaled volume estimates using median volume of each size category (left y-axis).

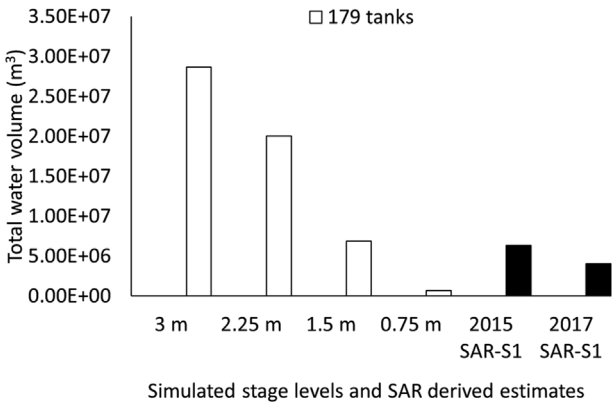


Fig. 14. Total water volume for 179 tanks with simulated fill levels at 3.0 m, 2.25 m, 1.5 m and 0.75 m using the TanDEM-X DEM and compared with actual 2015 and 2017 SAR-derived total storage estimate.

estimates from S1-A for the 179 tanks were compared with volume estimates for the 34-tank subset for each of the four stage levels. The simulated fill levels from the 34 tanks were estimated directly from the DEM and not using a power approximation. Recall that the 34-tank subset is from the previous 72 tanks that showed representative tank geometries. The simulated fill levels for the 179 tanks were estimated

using the DEM; the median volume of each size category of the 34 tanks was extracted and scaled to 179 tanks (see §4.3). While the 34-tank simulation is more accurate, it is only a small subset and therefore, the 179-tank median total volume estimates were also considered. While total volumes are a magnitude larger compared with median upscaled tank volumes, both the 34-tank simulation and the 179-upscaled volume estimates show the same pattern at the various fill levels indicating consistency in estimations (Fig. 13). As shown in Fig. 14, compared to simulated tank filling levels at the four fill level increments in Fig. 13, S1-A-estimated tank volumes from the power relationships for both years showed tanks filling closest to simulated stage level category of 1.5 m; they did not fill close to full simulated capacity (set at a stage of 3 m in this study).

5.3.2. Single tank volume estimate from multi-sensors

While the volume estimates retrieved using S1-A over larger spatial scales provided insight into the consistency of maximum water extent and potentially the stored water volume, the temporal sampling of the tanks by S1-A alone and the underestimation in tank SW area is insufficient to evaluate precise tank volume changes over time. Therefore, for test (2), a time-series of satellite-based volume estimates was calculated and shown for a selected tank in Fig. 15. This tank and observation year provide an example of a season with both cloud-free optical observations (PS, S2-A and L8) and S1-A data, for a Northeast monsoon season. The tank has a maximum SW area of 10–20 ha and therefore, the CAT 10–20 ha equation from Table 5 is used as the power model to retrieve volume estimates. All cloud-free observations from optical and SAR sensors covering the tank were retrieved for August 2017–January 2018.

Cloud-free tank volume estimates are shown in the main panel of

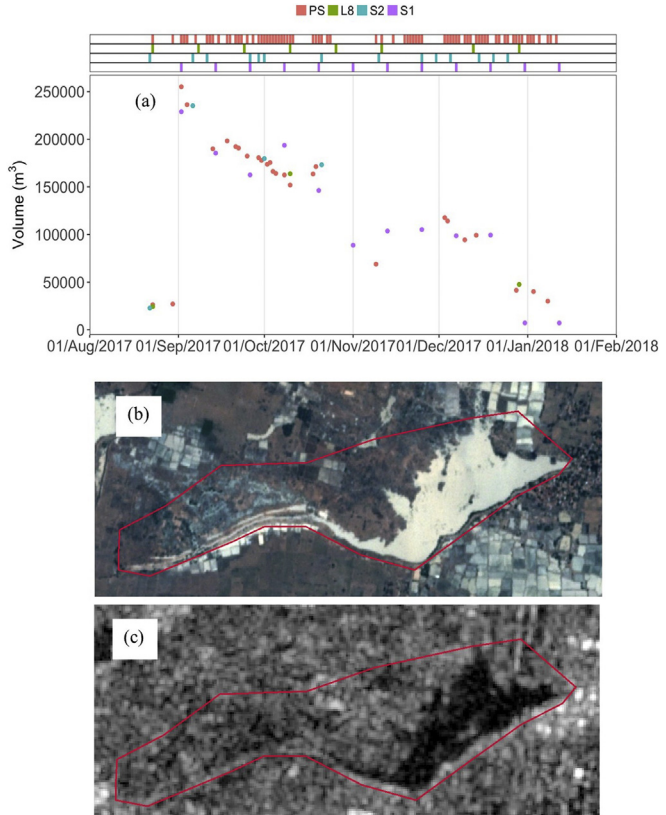


Fig. 15. (a) Time-series of volume estimates acquired from PS, L8, S2-A and S1-A, top bars show all available acquisition dates while the dots for each sensor show only the volume retrieved from cloud free observations. (b–c) show (b) PS TCC image and (c) S1-A VV polarized image during peak SW extent and volume in the season (see Sept 2, 2017 in plot a).

Fig. 15a with the coloured markers above the graph corresponding to scene acquisition dates, regardless of cloud contamination. While PS imagery is subject to variable cloud contamination, its high temporal resolution enables more frequent cloud-free observations than L8 and S2-A sensors and facilitates not only a single snapshot of the volume but the seasonal variation of tank water volume. PS provides 27 SW areas, compared to three, four and 12 from L8, S2-A, and S1-A, respectively. Water volumes in the tank rose sharply at the start of September following the monsoon rains, and then dropped over the next 3 months as water was discharged from the tank (**Fig. 15a**). **Fig. 15b–c** shows the tank on September 2 with observations from PS and S1-A, corresponding to the largest SW area of the tank for this season.

This application test highlights how combined satellite radar and frequent visible-infrared observations of SW can be used to monitor tanks regularly all year-round. Additionally, inferences about inflows and outflows could be made if multiple adjacent daily observations are available.

6. Discussion

6.1. Volume-area (V-A) model

DEM quality is a significant challenge for water inundation modeling, particularly in data-sparse areas where a lack of high-resolution topographic or ground truth data exists. Results reported in **Table 4** and **Fig. 7** show the performance of the novel TanDEM-X DEM for bathymetry retrieval, and demonstrates a strong potential to quantify tank bathymetry when compared to field GPS data. Ideally, the tank SWS should be calculated using its bathymetries. Even though the TanDEM-X DEM does provide full spatial coverage, it is impossible to obtain the reservoir bottom topographies for many tanks in the GRB because of dense vegetation presence in reservoir beds that limit error-free estimates. As a compromise, V-A power relationship(s) generated from a large subset ($n = 72$) tanks and radar and optical-delineated SW areas were proposed.

The TanDEM-X DEM product has set the foundation for evaluating simple, commonly applied, power type expressions for volume estimation in small storage structures (Karran et al., 2017; Liebe et al., 2005; Meigh, 1995; Sawunyama et al., 2006; Young et al., 2017). At the individual tank scale (*i.e.*, TS model), the results present significant power relationships between the storage volume and area for the 72 tanks – a predicted result, given the success of the previous studies and the expected over-fitting of the model when focused on independent tank structures. The parameter values of the GEN V-A relationship in **Table 5** for the GRB are in the same order of magnitude as those obtained for basins in Africa by Annor et al. (2009) and Liebe et al. (2005) for the Upper East Region of Ghana and by Sawunyama et al. (2006) for the Limpopo basin in Zimbabwe. The power equations reported in these studies are from 41, 21, and 12 reservoirs and fitted the data with b coefficients of 1.44, 1.44 and 1.33, respectively. Young et al. (2017) found higher b coefficients of 2.1 and 2.0, respectively when investigating only two tanks. In our study, high b coefficients greater than 1.8 were obtained for three TS models in the sample of 72. Similar to this study in terms of reservoir size and a large sample size, Rodrigues and Liebe (2013) used a power relationship to generate a and b parameters for 103 small reservoirs (1–40 ha) in two semi-arid watersheds. They also noted a high R^2 between the a and b parameters. More interestingly, and unpredictably, is the result showing high variability for a and b parameters among the 72 evaluated tanks and the substantial impact this variability introduces to volume estimates. It is an unpredictable result because common practice has been to develop a single regionalized V-A equation for geomorphologically similar landscapes, leading to the assumption of minimal variation among reservoirs. Our results highlight that variability among individual structures, even in geomorphologically similar landscapes, is important to consider when using a power type relationship, and when assessing a

baseline to compare volume estimates when further approximating the models (*i.e.* CAT and GEN). It is likely that previous studies have been unable to evaluate the former points due to limited bathymetric data. Fortunately, the TanDEM-X DEM facilitated the calculation of a dense set of bathymetric data for tanks, providing the ability to generate four power type models.

Prior to this research there was no RS-based method to estimate tank SWS in this region during monsoon periods: this is now possible with power law expressions and with estimated volume uncertainties. The application of the V-A relationship method revealed that at water levels below 1.5 m, volumes can be estimated within an absolute volume error range of 6–8% (TS, GEN and CAT models), with the CAT model providing the best solution according to the V_{ERR} method. By indicating the uncertainty for volume estimation, users can adopt our V-A relationship(s) approach and produce uncertainty estimates. This is important given that tanks normally do not fill to maximum and therefore the absolute error estimates from the V-A method are likely reduced at lower fill levels. The bund wall is highly variable in shape and size between reservoirs and approximating this region introduces more error as the water level increases. Some tanks in southern India have bunds larger than 3 m and also fill with water above our set maximum bund height (3 m). Our methodology is not applicable to such structures. While the bathymetric field data supported the use of TanDEM-X DEM data, it is unknown if this is the case for tanks in the lower basin because the monsoon regime is typically variable across the basin. Since the TanDEM-X DEM is from RS observations spanning a five-year period, some scenes incorporated in the generation of the DEM may have been acquired when tanks contained water, contributing to differences in bathymetry values (Collins et al., 2015). To better understand these differences arising from the presence of water, a bathymetric survey should be completed on an expanded representative number of tanks in the middle and lower basin.

6.2. Delineation of reservoir surface water (SW) extent

SW extent estimates from multi-source RS observations combined with V-A relationships provide an opportunity to estimate water volume in tank structures from satellite SW extent alone. While S1-A is more suitable for tank monitoring compared with visible-infrared satellite observations during cloudy conditions, high DAI differences between PS SW and S1-A SW extent are produced by limitations of S1-A for SW extent estimates of small irrigation structures. Water-land inseparability is likely caused by the influence of water surface roughness and vegetation presence on backscatter intensity, in combination with the lower spatial resolution of S1-A compared with PS. To improve the accuracy of S1-A extractions of SW extent, the incorporation of a shape metric (S_t) to eliminate SW areas that are too narrow to be accurately detected is suggested. In addition, the development of an inventory of active tank SW extents for a high precipitation year from PS data would eliminate tanks unsuitable for monitoring using S1-A.

In this study, a tank mask was used to constrain the estimation of SW area using S1-A. However, to apply the volume estimation method to a larger number of tanks, either a vector dataset of tank boundaries is needed for a larger number of tanks or the methodology for S1-A SW estimation needs to be improved to ensure that only open water areas are detected. The latter is a non-trivial problem because when water pools start forming in the fields surrounding the tanks, the land-water contrast deteriorates causing problems for tank SW area extraction using S1-A and also PS with only four spectral bands (Eilander, Annor, Iannini and van de Giesen, 2014). SW detection using Otsu was suitable in this study for basin wide SW estimation because tanks were observed at maximum seasonal SW extent, which corresponded to a bimodal distribution between water and adjacent land pixels; a condition required for Otsu to perform well. However, when monitoring for a full season, a more rigorous SW extraction methodology should be implemented. This is because towards the end of the season when

reservoir SW extents shrink, the distribution between water and land pixels is no longer bimodal, potentially decreasing the accuracy of the SW classification. This result has previously been shown by Liebe et al. (2009) and was also demonstrated in the single tank volume time-series estimates; notable were the changes in water volume in a few days, likely unrelated to natural variations (rainfall and evaporation) or human-induced but rather to SW estimation errors from S1-A under these conditions.

6.3. Monitoring storage - two applications examples

Prior to the availability of the TanDEM-X DEM data, tank SWS was evaluated by examining the spectral response of water from Landsat reflectance observations to approximate water depth (Mialhe et al., 2008). While this work was important in developing the application of RS to support understanding of tank structures, their method does not facilitate monitoring tanks during monsoon periods when they are habitually cloud covered, or when tank water is turbid. The two application examples in this study demonstrate the ability to monitor tank volumes with V-A relationships and multi-sensor SW estimates. The enhanced global TanDEM-X DEM along with high frequency and accurate SW observations from CubeSats, provide the ability for a more comprehensive hydrological analysis based on RS observations, with potential implications for water security in semi-arid environments. Yet, uncertainties remain about the hydrological dynamics of these small irrigation reservoirs from RS estimates of water volumes. For example, for the GRB scale S1-A volume estimates, both the observed years are an underestimation of the total input to the GRB's water budget since functioning tanks can fill unobserved multiple times during the season, plus water may be lost through hydrologic processes that are not captured by infrequent state observations from space. Nevertheless, the fact that the 2017 estimated fill levels were lower than the 2015 levels agrees with the lower basin-wide precipitation in 2017 estimated from the CHIRPS data.

The PS data were invaluable for augmenting the observation frequency of S1-A to continuous (~5 day) monitoring. However, there are challenges that remain prior to using CubeSat for large scale hydrological observing of tank structures. These challenges, noted by Cooley et al. (2017), and further highlighted in our work, include the difficulty of automating the SW classification with only four spectral bands and the time-consuming radiometric calibration required between scenes. The use of an object-based SW estimate for volume conversion is a critical methodology step to mitigate geolocation error propagating into the SW estimates. A threshold using only NDWI was suitable to distinguish water from land due to restricting the analysis to minimal cloud covered PS scenes and an environment with few landscape surfaces to be spectrally confused with water. The PS sensors only sample between 455 and 860 nm and therefore do not include a short-wave infrared band, which restricts the PS data application to environments where snow and ice do not need to be distinguished from open surface water.

Despite these limitations, with over 160,000 of these structures present in southern India, the hydrological potential of tank systems to store water for managed use is extremely important (Vaidyanathan, 2001). This study could have significant societal benefit by improving the prediction and application of irrigation in marginalized rural communities in southern India which are threatened with lasting climate extremes. Water volume extraction methods developed in this work could be incorporated into hydrological and crop management frameworks to evaluate water requirements under current and future climate scenarios. Additionally, the Surface Water and Ocean Topography (SWOT) mission, to be launched in 2020, is expected to provide the first application of satellite altimetry for tanks and could be incorporated into our tank monitoring methodology by providing water levels at a higher temporal and spatial resolution.

7. Conclusion

Tank systems potentially reduce water stress in southern India by providing local groundwater recharge and surface-accessible water during the dry seasons. We demonstrate RS techniques for tank monitoring that provide an opportunity to better understand the dominant hydrologic controls governing reservoir outflow and inflows. A methodology is developed to monitor and quantify water volume in tanks in southern India under all weather conditions, using S1-A observations and high-resolution PS data. Our results couple empirical V-A models and remotely sensed SW area estimates and is a promising first step and proof-of-concept toward predicting ungauged flows in tanks. As developments in cloud computing for RS continue, our method can be expanded to larger areas. The ability to estimate reservoir volumes using satellite RS has wide reaching implications in transboundary water management. Remotely sensed observations of tank volumes could assist stakeholders in making more informed decisions about water management issues related to tank use. Since small irrigation structures are not continuously monitored, our findings represent a unique contribution to the hydrologic science community.

Acknowledgements

The authors acknowledge the support from the Natural Science and Engineering Council's Discovery Grant program, seed funding from the University of Waterloo's International Research Partnerships Grant, and from DLR (Germany) for access to TanDEM-X DEM data under the successful proposal DEM_HYDR0751. The authors also thank the five anonymous RSE reviewers and the RSE editorial team for their constructive comments that helped us to improve the quality of the manuscript. We also thank the DHAN Foundation for generously sharing their experiences and helping facilitate field data collection.

References

- Alsdorf, D.E., Rodríguez, E., Lettenmaier, D.P., 2007. Measuring surface water from space. *Rev. Geophys.* 45, 1–24.
- Annor, F.O., van de Giesen, N., Liebe, J., van de Zaag, P., Tilmant, A., Odai, S.N., 2009. Delineation of small reservoirs using radar imagery in a semi-arid environment: a case study in the upper east region of Ghana. *Phys. Chem. Earth* 34, 309–315.
- Baup, F., Frappart, F., Maubant, J., 2014. Combining high-resolution satellite images and altimetry to estimate the volume of small lakes. *Hydrol. Earth Syst. Sci.* 18, 2007–2020.
- Behnamian, A., Banks, S., White, L., Brisco, B., Millard, K., Pasher, J., Chen, Z., Duffe, J., Bourgeau-chavez, L., Battaglia, M., 2017. Semi-automated surface water detection with synthetic aperture radar Data: a wetland case study. *Remote Sens.* 9, 1–21.
- Bioresita, F., Puissant, A., Stumpf, A., Malet, J., 2018. A method for automatic and rapid mapping of water surfaces from sentinel-1 imagery. *Remote Sens.* 10, 1–17.
- Bitterman, P., Tate, E., Van Meter, K.J., Basu, N.B., 2016. Water security and rainwater harvesting: a conceptual framework and candidate indicators. *Appl. Geogr.* 76, 75–84.
- Bolanos, S., Stiff, D., Brisco, B., Pietroniro, A., 2016. Operational surface water detection and monitoring using Radarsat 2. *Remote Sens.* 8, 285.
- Bonnema, M., Hossain, F., 2017. Inferring reservoir operating patterns across the Mekong Basin using only space observations. *Water Resour. Res.* 53, 3791–3810.
- Clement, M.A., 2018. Multi-temporal synthetic aperture radar flood mapping using change detection. *Flood Risk Manag* 11, 152–168.
- Collins, J., Riegler, G., Schrader, H., Tinz, M., 2015. Applying terrain and hydrological editing to TanDEM-X data to create a consumer-ready worlddem product. *Photogramm. Remote Sens.* 40, 1149–1154.
- Cooley, S.W., Smith, L.C., Ryan, J.C., Pitcher, L.H., Pavelsky, T.M., 2019. Arctic-boreal lake dynamics revealed using CubeSat imagery. *Geophys. Res. Lett.* 46, 2111–2120.
- Cooley, S.W., Smith, L.C., Stepan, L., Mascaro, J., 2017. Tracking dynamic northern surface water changes with high-frequency F CubeSat imagery. *Remote Sens.* 9, 1306.
- Döll, P., Fiedler, K., Zhang, J., 2009. Hydrology and Earth System Sciences Global-scale analysis of river flow alterations due to water withdrawals and reservoirs. *Hydrol. Earth Syst. Sci.* 13, 2413–2432.
- Du, Y., Zhang, Y., Ling, F., Wang, Q., Li, W., Li, X., 2016. Water bodies' mapping from Sentinel-2 imagery with Modified Normalized Difference Water Index at 10-m spatial resolution produced by sharpening the swir band. *Remote Sens.* 8.
- Eilander, D.M., Annor, F.O., Iannini, L., van de Giesen, N., 2014. Remotely sensed small reservoir monitoring: a Bayesian approach. *Remote Sens.* 6, 1191–1210.
- Eineder, M., Adam, N., Bamler, R., Yague-Martinez, N., Breit, H., 2009. Spaceborne spotlight SAR interferometry with TerraSAR-X. *IEEE Trans. Geosci. Remote Sens.* 47, 1524–1535.

- Eineder, M., Fritz, T., Abdel Jaber, W., Rossi, C., Breit, H., 2012. Decadal Earth topography dynamics measured with TanDEM-X and SRTM. International Geoscience and Remote Sensing Symposium. IGARSS), pp. 1916–1919.
- Gao, H., Birkett, C., Lettenmaier, D.P., 2012. Global monitoring of large reservoir storage from satellite remote sensing. *Water Resour. Res.* 48, 1–12.
- Gorelick, N., Hancher, M., Dixon, M., Ilyushchenko, S., Thau, D., Moore, R., 2017. Google Earth engine: planetary-scale geospatial analysis for everyone. *Remote Sens. Environ.* 202, 18–27.
- Huang, C., Chen, C., Zhang, S., Wu, J., 2018. Reviews of geophysics detecting, extracting, and monitoring surface water from space using optical sensors: a review. *Rev. Geophys.* 56, 333–360.
- Karran, D.J., Westbrook, C.J., Wheaton, J.M., Johnston, C.A., Bedard-haughn, A., 2017. Rapid surface-water volume estimations in beaver ponds. *Hydrol. Earth Syst. Sci.* 21, 1039–1050.
- Liebe, J., van de Giesen, N., Andreini, M., 2005. Estimation of small reservoir storage capacities in a semi-arid environment A case study in the Upper East Region of Ghana. *Phys. Chem. Earth* 30, 448–454.
- Liebe, J., van de Giesen, N., Andreini, M.S., Steenhuis, T.S., Walter, M.T., 2009a. Suitability and limitations of ENVISAT ASAR for monitoring small reservoirs in a semiarid area. *IEEE Trans. Geosci. Remote Sens.* 47, 1536–1547.
- Liebe, J., van de Giesen, N., Andreini, M., Walter, M.T., Steenhuis, T.S., 2009b. Determining watershed response in data poor environments with remotely sensed small reservoirs as runoff gauges. *Water Resour. Res.* 45, 1–12.
- Magome, J., Ishidaira, H., Takeuchi, K., 2003. Method for satellite monitoring of water storage in reservoirs for efficient regional water management. *Water Resour. Res.* 303–310.
- Martinis, S., Plank, S., 2018. The use of sentinel-1 time-series data to improve flood monitoring in arid areas. *Remote Sens.* 10, 1–13.
- Meigh, J., 1995. The impact of small farm reservoirs on urban water supplies in Botswana. *Nat. Resour. Forum* 19, 71–83.
- Messenger, M.L., Lehner, B., Grill, G., Nedeva, I., Schmitt, O., 2016. Estimating the volume and age of water stored in global lakes using a geo-statistical approach. *Nat. Commun.* 7, 1–11.
- Mialhe, F., Gunnell, Y., Mering, C., 2008. Synoptic assessment of water resource variability in reservoirs by remote sensing: general approach and application to the runoff harvesting systems of south India Franc. *Water Resour. Res.* 44, 1–14.
- Minke, A.G., Westbrook, C.J., van der Kamp, G., 2010. Simplified volume-area-depth method for estimating water storage of prairie potholes. *Wetlands* 30, 541–551.
- Otsu, N., 1979. A threshold selection method from gray-level histograms. *IEEE Trans. Syst. Man Cybern.* 9, 62–66.
- Palanisami, K., Meinzen-Dick, R., Giordano, M., 2010. Climate change and water supplies: options for sustaining tank irrigation potential in India. *Econ. Pol. Wkly.* 45, 183–190.
- Pekel, J.-F., Cottam, A., Gorelick, N., Belward, A.S., 2016. High-resolution mapping of global surface water and its long-term changes. *Nature* 540, 418–422.
- Planet Team, 2019. Planet Application Program Interface: in Space for Life on Earth. Planet: San 1003 Francisco, CA, USA, pp. 2019.
- Reddy, V.R., Reddy, M.S., Palanisami, K., 2018. Tank rehabilitation in India: review of experiences and strategies. *Agric. Water Manag.* 209, 32–43.
- Rodrigues, L.N., Sano, E.E., Steenhuis, T.S., Passo, D.P., 2012. Estimation of small reservoir storage capacities with remote sensing in the Brazilian Savannah region. *Water Resour. Manag.* 26, 873–882.
- Rodrigues, L.N., Liebe, J., 2013. Small reservoirs depth-area-volume relationships in Savannah Regions of Brazil and Ghana. *Water Resour. Irrig. Manag.* 2, 1–10.
- Sawunyama, T., Senzanje, A., Mhziba, A., 2006. Estimation of small reservoir storage capacities in Limpopo River Basin using geographical information systems (GIS) and remotely sensed surface areas: case of Mzingwane catchment. *Phys. Chem. Earth* 31, 935–943.
- Sayl, K.N., Muhammad, N.S., El-Shafie, A., 2017. Optimization of area-volume-elevation curve using GIS-SRTM method for rainwater harvesting in arid areas. *Environ. Earth Sci.* 76, 1–10.
- Torres, R., Snoeij, P., Geudtner, D., Bibby, D., Davidson, M., Attema, E., Potin, P., Rommen, B.Ö., Flouri, N., Brown, M., Traver, I.N., Deghaye, P., Duesmann, B., Rosich, B., Miranda, N., Bruno, C., L'Abbate, M., Croci, R., Pietropaolo, A., Huchler, M., Rostan, F., 2012. GMES Sentinel-1 mission. *Remote Sens. Environ.* 120, 9–24.
- Vaidyanathan, A. (Ed.), 2001. Tanks of South India. Centre for Science and Environment, Delhi.
- van Bemmelen, C.W.T., Mann, M., de Ridder, M.P., Rutten, M.M., van de Giesen, N.C., 2016. Determining water reservoir characteristics with global elevation data. *Geophys. Res. Lett.* 43 (11), 278 11,286.
- Van Den Hoek, J., Getirana, A., Jung, H.C., Okeowo, M.A., Lee, H., 2019. Monitoring reservoir drought dynamics with landsat and radar/lidar altimetry time series in persistently cloudy eastern Brazil. *Remote Sens.* 11.
- Van Meter, K.J., Steiff, M., McLaughlin, D.L., Basu, N.B., 2016. The socioecohydrology of rainwater harvesting in India: understanding water storage and release dynamics across spatial scales. *Hydrol. Earth Syst. Sci.* 20, 2629–2647.
- Verpoorter, C., Kutser, T., Seekell, D.A., Tranvik, L.J., 2014. A global inventory of lakes based on high-resolution satellite imagery. *Geophys. Res. Lett.* 41, 6396–6402.
- Vörösmarty, C.J., Green, P., Salisbury, J., Lammers, R.B., 2000. Global water Resources: vulnerability from climate change and population growth contemporary population relative to demand per discharge. *Science* 289, 284–288.
- Vörösmarty, C.J., McIntyre, P.B., Gessner, M.O., Dudgeon, D., Prusevich, A., Green, P., Glidden, S., Bunn, S.E., Sullivan, C.A., Liermann, C.R., Davies, P.M., 2010. Global threats to human water security and river biodiversity. *Nature* 467, 555–561.
- Wang, Y., Yésou, H., 2018. Remote sensing of floodpath lakes and wetlands: a challenging frontier in the monitoring of changing environments. *Remote Sens.* 10, 1955.
- Wessel, B., Huber, M., Wohlfart, C., Marschalk, U., Kosmann, D., Roth, A., 2018. Accuracy assessment of the global TanDEM-X digital elevation model with GPS data. *ISPRS J. Photogrammetry Remote Sens.* 139, 171–182.
- Yan, K., Di Baldassarre, G., Solomatine, D.P., Schumann, G.J.P., 2015. A review of low-cost space-borne data for flood modelling: topography, flood extent and water level. *Hydrol. Process.* 29, 3368–3387.
- Young, S., Peschel, J., Penny, G., Thompson, S., Srinivasan, V., 2017. Robot-assisted measurement for hydrologic understanding in data sparse regions. *Water* 9, 494.
- Zhang, S., Foerster, S., Medeiros, P., de Araújo, J.C., Motagh, M., Waske, B., 2016. Bathymetric survey of water reservoirs in north-eastern Brazil based on TanDEM-X satellite data. *Sci. Total Environ.* 571, 575–593.